

Dark matter and visible baryons in M33

Edvige Corbelli

Osservatorio Astrofisico di Arcetri, Largo E. Fermi, 5 I-50125 Firenze, Italy

Received ; accepted

ABSTRACT

In this paper we present new measurements of the gas kinematics in M33 using the CO J=1-0 line. The resulting rotational velocities complement previous 21-cm line data for a very accurate and extended rotation curve of this nearby galaxy. The implied dark matter mass, within the total gaseous extent, is a factor 5 higher than the visible baryonic mass. Dark matter density profiles with an inner cusp as steep as R^{-1} , suggested by some numerical simulation of structures formation, are compatible with the actual data. The dark matter concentrations required for fitting the M33 rotation curve are very low but still marginally consistent with halos forming in a standard Cold Dark Matter cosmology. The M33 virialized dark halo is at least 50 times more massive than the visible baryons and its size is comparable with the M33-M31 separation. Inner cusps as steep as $R^{-1.5}$ are ruled out, while halo models with a large size core of constant density are consistent with the M33 data. A central spheroid of stars is needed and we evaluate its dynamical mass range. Using accurate rotational velocity gradients and the azimuthally averaged baryonic surface densities, we show that a disk instability can regulate the star formation activity in M33. Considering the gaseous surface density alone, the predicted outer star formation threshold radius is consistent with the observed drop of the H- α surface brightness if a shear rate criterion is used with the lowest possible value of velocity dispersion. The classical Toomre criterion predicts correctly the size of the unstable region only when the stellar or dark halo gravity, derived in this paper, is added to that of the gaseous disk.

Key words: galaxies:individual:M33 - ISM:molecules - galaxies:kinematics and dynamics - galaxies:halos - dark matter - stars:formation

arXiv:astro-ph/0302318v1 17 Feb 2003

1 INTRODUCTION

M33 is a low luminosity spiral galaxy in the Local Group. Its large angular extent and well determined distance make it ideal for a detailed study of the radial distribution of visible and dark matter. The interplay between the dark and visible matter as well as the nature and the radial distribution of dark matter are still open crucial issues with strong implications for galaxy formation and evolution theories. M33 has three advantages over its brighter neighbor M31: *(i)* being of lower luminosity, it is a dark matter dominated spiral in which it is easier to disentangle the dark and luminous mass components (Persic, Salucci & Stel 1996, Corbelli & Salucci 2000 hereafter CS); *(ii)* it has no prominent black hole or bulge component in the center (Gebhardt et al. 2001) and therefore it can be used to test if the innermost dark matter density profile is consistent with cosmological models which predict a central density cusp; *(iii)* being at lower declination, high sensitivity 21-cm observations with the Arecibo radio telescope made possible a velocity field map out to large galactocentric radii. CS have used this velocity field map, together with aperture synthesis data of Newton (1980) and with the tilted ring model results of Corbelli & Schneider (1997), to derive the rotation curve of M33 out to 13 disk scalelengths. This unveiled large scale properties of the mass distribution in M33, such as the lack of correlation between the dark and visible matter, the dark halo mass and the possible radial slope of the dark matter density. However some ambiguities are left, especially in the inner regions, where the low spatial resolution of 21-cm observations and the possible role of a stellar nucleus or of the molecular gas component have not allowed to establish unambiguously the steepness of the dark matter density profile.

Several authors, e.g. Bolatto et al. (2002), have shown the advantages of using CO observations for determining the central densities of dark matter halos. A full map of the CO emission in M33 would not only provide higher spatial resolution data on the velocity field but it would also give a first estimate of the molecular mass distribution in this galaxy. The very blue color of M33 and the presence of prominent HII regions indicate vigorous star formation activity in the nuclear region and along the spiral arms: here the molecular gas component might represent a substantial fraction of the total disk mass. CO observations of the innermost 500 pc of M33 (Wilson & Scoville 1989), have confirmed in fact that here the molecular gas has a higher surface density than the atomic gas. Recently Heyer, Corbelli & Schneider (2003) have fully mapped the CO emission in M33 using the FCRAO 14-m telescope. A detailed analysis of the molecular gas distribution and emission features will be presented elsewhere. In this paper we derive only the average radial distribution of the molecular gas mass (Section 2) and analyze the kinematics of the CO gas (Section 3). The implications for the dark matter halo models are shown in Section 4. An accurate knowledge of the velocity field and of the mass surface densities over a large disk area are useful for understanding the processes which trigger the star formation in this galaxy, such as disk instabilities, spiral arms, cooling and heating mechanisms. A possible link between the radial extent of the observed star formation region and the gravitationally unstable region in the disk is discussed in Section 5.

2 THE MOLECULAR DATA

The nearby spiral galaxy M33 has been fully mapped in the CO J=1-0 transition with a velocity resolution of 0.81 km s^{-1} and a spatial resolution of 45 arcsec using the FCRAO 14-m telescope (Heyer, Corbelli & Schneider 2003). A 22.5 arcsec spatial sampling is obtained over an area of about 900 arcmin^2 centered on RA $01^{\text{h}}33^{\text{m}}50^{\text{s}}.89$ and DEC $30^{\circ}39'36''.7$. For a distance to M33 of 0.84 Mpc (Freedman et al. 2001), which will be used throughout this paper, this means that the total disk area observed is about 44 kpc^2 at a spatial resolution of 165 pc. Here we shall use the data at the original spatial and spectral resolution to derive the kinematical information on the molecular gas. We analyze in detail each spectrum by assigning a spectral window $\Delta V = V^f - V^i$ to any detectable emission feature. There are a few cases where more than one spectral window is needed but secondary signals are always quite low. If no emission is clearly present in a given spectrum, a spectral window is set based on the diffuse emission detectable when averaging nearby positions. We compute the integrated brightness temperature F in K km s^{-1} by integrating over ΔV the telescope temperature observed at each position in the sky, and dividing this number by the main beam efficiency of the telescope (which is 0.45 at 115 GHz). In order to derive the average radial distribution of the molecular gas we need a concentric ring model. 45 concentric rings of width 150 pc cover all the M33 surface area observed. They are tilted as to best fit the neutral hydrogen distribution (Corbelli & Schneider 1997). Inside this area the position angle of the best fitting ring model changes only slightly, and therefore we consider it constant and equal to 22° . The inclination of the rings increases from 50° to 58° moving radially outwards, as described in details in Section 3 of CS. We use the concentric ring model for assigning a face on radial distance to each observed position, and for deriving the inclination corrected average flux in each ring. Following Wilson's results (Wilson 1995) we use the standard conversion factor between the CO luminosity and the line of sight column density of H_2 ($S_{H_2} = 2.8 \times 10^{20} \times F \text{ cm}^{-2} = 4.5 \times F \text{ M}_{\odot} \text{ pc}^{-2}$).

The resulting average surface density of molecular hydrogen, perpendicular to the plane of the galaxy (i.e. corrected for the disk inclination respect to our line of sight), is shown in Figure 1. The estimated total mass of molecular gas is $2 \times 10^8 \text{ M}_{\odot}$. This is a factor 6 higher than measured by Wilson & Scoville (1989) in the smaller nuclear region. The molecular hydrogen mass is about 10% the neutral hydrogen mass ($2.2 \times 10^9 \text{ M}_{\odot}$ for $D=0.84 \text{ Mpc}$). The surface density distribution does not peak

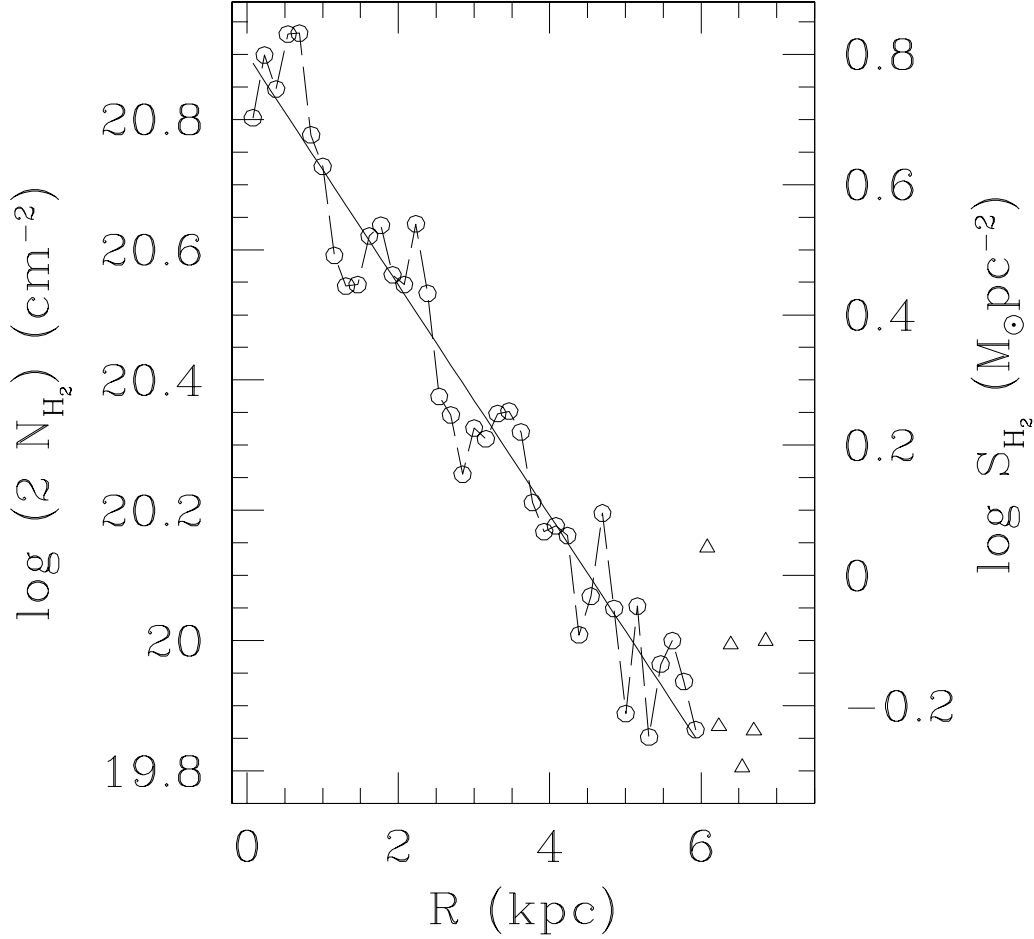


Figure 1. Average surface density of molecular hydrogen as a function of R in the plane of the M33 disk. The straight line is the best fit to all data with $R < 6$ kpc (open dots). Larger radii were only partially covered by our survey.

at the center but shows a peak at a few hundred parsecs from the nucleus, as noted previously by Wilson & Scoville (1989). The most prominent CO emission features are located in the innermost 1 kpc region and along the spiral arms. This can be seen already in the $1.3 \times 7 \text{ kpc}^2$ preliminary emission map (Corbelli 2000) oriented along the M33 major axis. An exponential is fitted to the azimuthally averaged surface density data from 0 to 6 kpc. We leave out from the fit the last 6 points shown in Figure 1 which seem to indicate a plateau at the level of $0.6 M_{\odot} \text{pc}^{-2}$. In reality we don't have enough sensitivity and coverage in our survey to determine the slope of the H_2 distribution so far out. The best fit to S_{H_2} is shown by the straight line in Figure 1 and is given by

$$S_{H_2} = 6.3 \times \exp\left(-\frac{R}{2.5 \text{ kpc}}\right) M_{\odot} \text{pc}^{-2} \quad (1)$$

Therefore the CO radial scalelength in M33 is larger than the B and K band scalelengths (1.9 and 1.3 kpc respectively, Regan & Vogel 1994). In Figure 2 we show the HI as well as the total (HI + H_2) gas distribution in this galaxy. The total gas surface density can be described by a gaussian profile with half width at half maximum of about 6 kpc. Note that the bump of the spiral arm feature around 2 kpc is visible in the azimuthal averages of the molecular and atomic gas shown in Figure 2.

3 THE CO ROTATION CURVE

As Wilson & Scoville (1989) have already pointed out from a comparison of interferometric and single dish data, small clouds and diffuse emission in M33 contain a non negligible fraction of the total molecular mass. Half of the molecular gas mass that we estimate in M33 resides in fact in regions with integrated flux less than $3F_{\sigma} \simeq 1.33 \text{ K km s}^{-1}$. F_{σ} is the integrated noise defined in terms of the spectral window ΔV as:

$$F_{\sigma} = \sigma_{rms} \times \sqrt{\Delta V \times 0.81} \quad (2)$$

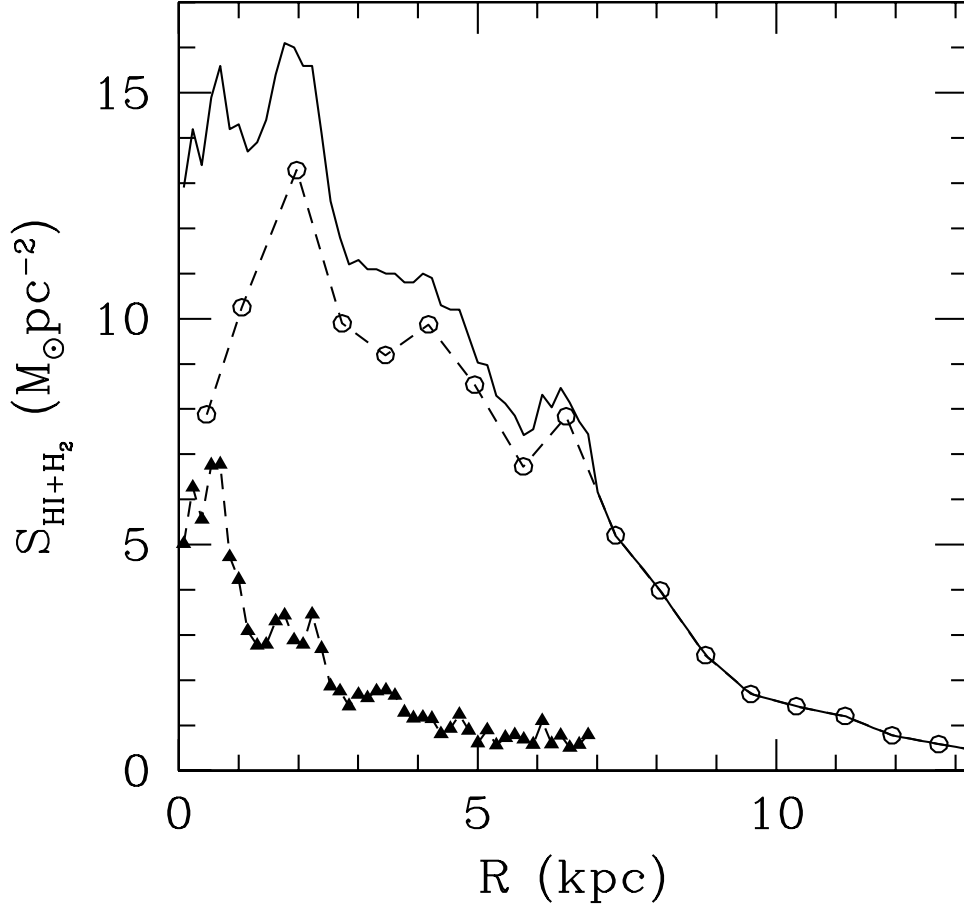


Figure 2. Average surface density of molecular hydrogen (filled triangles) and of atomic hydrogen (open circles) as a function of R in the plane of the M33 disk. The solid line is the sum of the two surface densities.

where σ_{rms} is the noise in the spectrum at the original resolution of 0.81 km s^{-1} . We fit single or double gaussians to all signals with integrated flux $F > F_{5\sigma}$ with a success rate of 75%. There is no significant shift between the gaussian and the flux weighted mean velocities (difference is $\lesssim 2 \text{ km s}^{-1}$ and is never above 5 km s^{-1}). In deriving kinematical informations we shall consider only spectra with $F > 5F_{\sigma}$, well fitted by gaussian profiles, from positions at angles $\alpha < 45^\circ$ from the major axis. These conditions restrict the analysis to a smaller radial range than observed. Luckily the prominent CO features come from locations close to the major axis and therefore we do have many points to average for building up a rotation curve. Corrections for the inclination of the disk and for the angle α between the spectrum position and the major axis are applied according to the tilted ring model described in the previous Section. Radial bin averages of the flux weighted mean velocities are plotted in Figure 3, also for the northern and southern side of the galaxy separately. Error bars in each bin show the dispersion of the velocities about the mean.

In the innermost 1 kpc the south and north rotation curves coincide reasonably well. Beyond this radius there are some differences both in the dispersions and in the mean values of V . Velocities in the southern half of M33 have higher dispersion than in the northern half. Also the southern side shows more clearly wiggles which can be interpreted as signs of density wave perturbations associated with the spiral arms. The detection of such features in the northern side is more doubtful. Residual velocities, obtained by subtracting the average rotational velocity $V(R)$ from the rotational velocity measured in each spectrum, $V_{obs}(R)$, are shown in Figure 4. In the left hand panel of Figure 4 the map of residual velocities is superimposed to the used tilted ring model, after rotating the galaxy by 22° clockwise in the plane of the sky. Cross and square symbols are for positive and negative residuals respectively, and their size is proportional to the amplitude of the residual velocities. Since the approaching side of the galaxy is the northern side ($y > 0$), a positive residual there means that the local velocity is less than the average rotational velocity. For each quadrant of the galaxy, the right hand panels of Figure 4 show the residual velocities as function of the galactocentric radius. It hard to judge whether there are signs of non circular motions and spiral density waves in the velocity residuals map. Part of the difficulty is due to the fact the bulk of the CO emission comes from

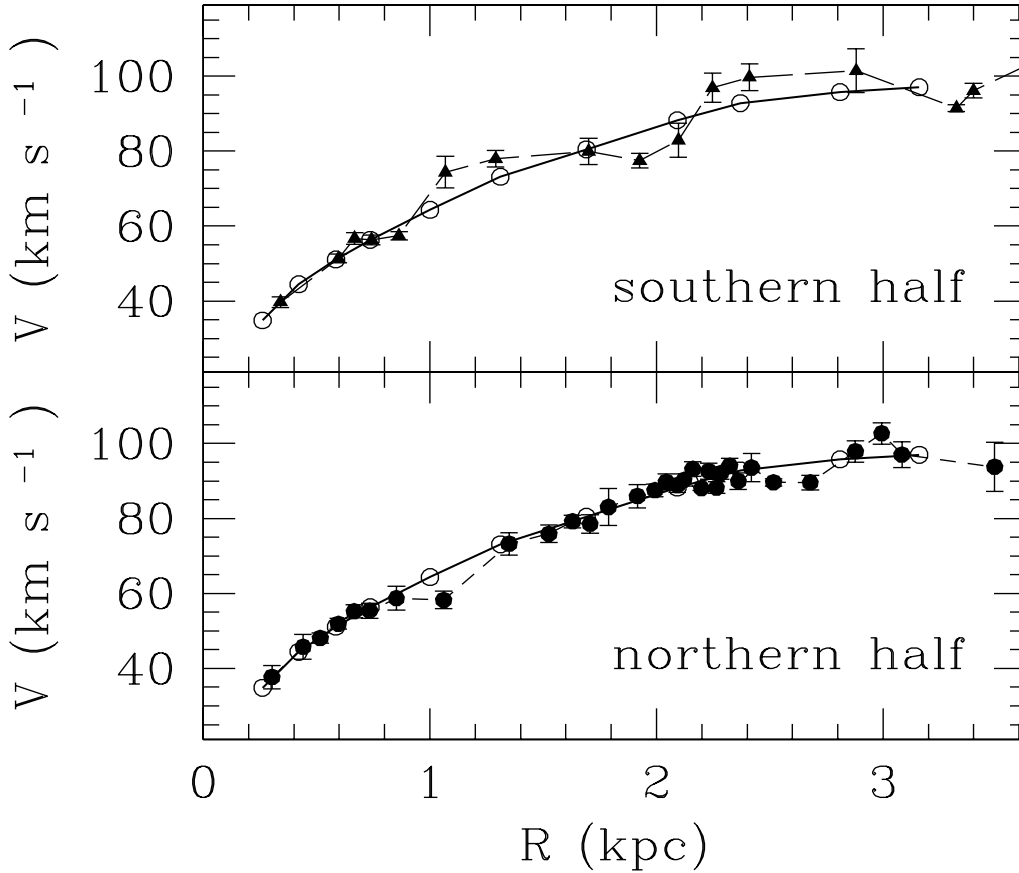


Figure 3. The northern and southern half data after averaging 10 adjacent points in each radial bin. Error bars show the dispersion in each bin. The rotation curve derived from averaging the northern and southern data is shown with open circles connected by a heavy solid line.

localized regions and is not smoothly distributed throughout the disk. A better attempt can be made in the future with the use of a numerical simulation for any given model assumption.

Comparison of the rotation curve in Figure 3 with the 21-cm data of Newton (1980) enlightens a discrepancy in the northern inner region, where at $R \lesssim 0.5$ kpc the HI velocities are lower by about 10 km s^{-1} than the CO velocities. This might be due to the lack of atomic gas in the innermost region, which together with the larger 21-cm beam, limits the accuracy of the atomic line measure. Finite angular resolution is not affecting significantly the velocities measured in our CO survey. To estimate any possible “beam smearing” effect we assume that the true velocity, for a given mass model, is that resulting from rotation curve and perform a numerical simulation to derive the observed velocities (van den Bosch & Swaters 2001). The observed velocities at each position on the plane of the sky are the flux weighted means of the rotational velocities along the line of sight, corrected for the assumed ring model and convolved with the shape of the telescope beam. We then compare the binned data with equally binned values of the velocities resulting from the simulation (we exclude points which form an angle $\alpha > 45^\circ$ with the major axis). Differences between the observed and the true velocities, for mass models which give a good fit to the data, are always smaller than 0.6 km s^{-1} except in the innermost 0.5 kpc where the beam smearing effect can lower the observed velocity as much as 2 km s^{-1} .

4 THE MASS COMPONENTS AND CONSTRAINTS ON COSMOLOGICAL HALO MODELS

Rotational velocities, which we use to derive the visible and dark matter distributions in M33, are shown in Figure 5. The innermost point at $R \simeq 150$ pc is from $\text{H}\alpha$ measurements of Rubin & Ford (1985). Our CO data extending over the interval $0.2 \leq R < 3.4$ kpc have been averaged into the subsequent 11 bins. For $3.4 \leq R < 5.5$ kpc data are taken from 21-cm observations of Newton (1980) at the Cambridge Half-Mile telescope while for larger radii we use Arecibo 21-cm data (CS and references therein). The plotted error bars in each bin are twice the dispersion of the velocities about the mean.

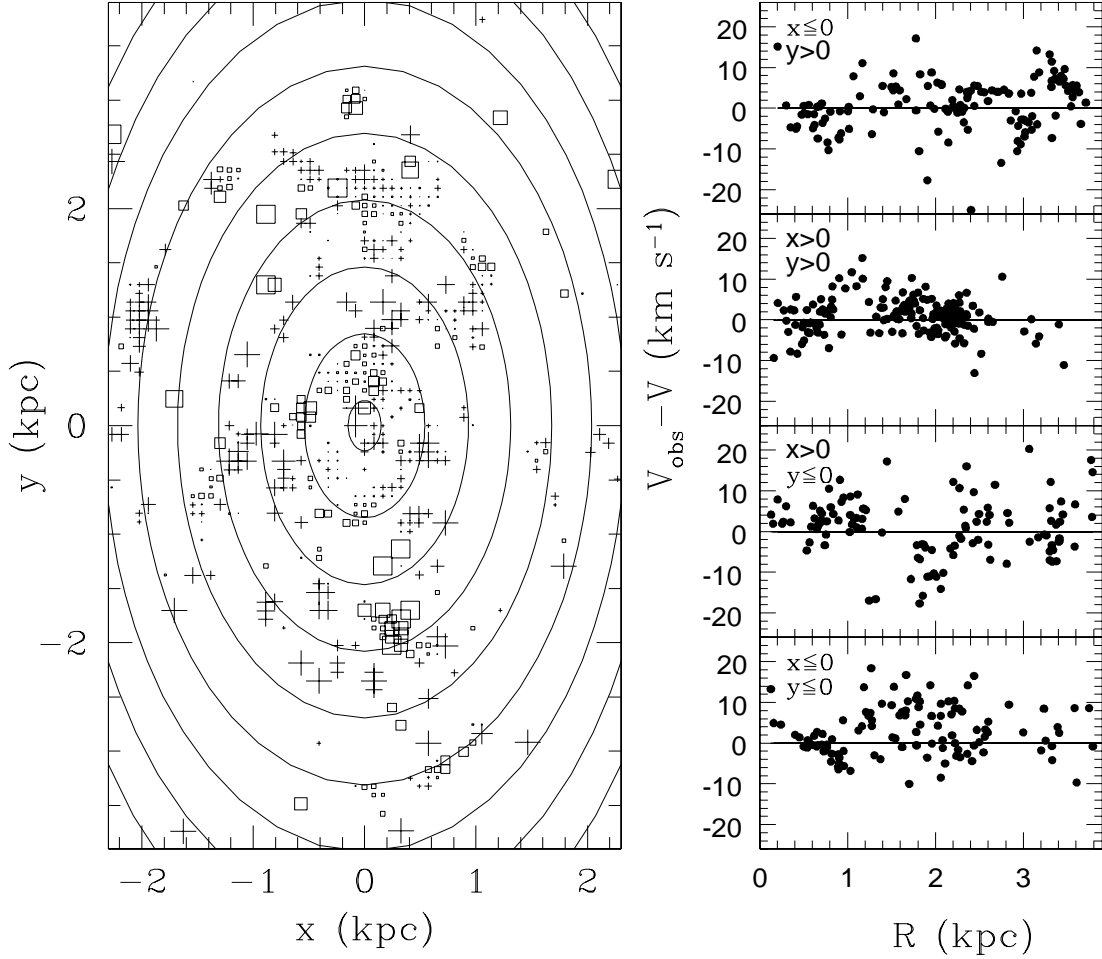


Figure 4. The left hand panel shows the map of the residual velocities, $V_{obs} - V$, where V is the average rotational velocity at R . It is superimposed to the used tilted ring model, after rotating the galaxy by 22° clockwise in the plane of the sky. Cross and square symbols are for positive and negative residuals respectively. The size of the symbols is proportional to the amplitude of the residuals. In the right hand panels of Figure 4 the residual velocities are shown as function of galactocentric radius in each quadrant of the galaxy.

We consider the dynamical contribution of two visible mass components: stars, distributed in a disk and in the nucleus, and gas, in molecular and in neutral atomic form. For the stellar disk we consider that the mass follows the light distribution in the K-band, well fitted by an exponential with scalelength $R_d \sim 1.3 \pm 0.2$ kpc (Regan & Vogel 1994). After subtracting the exponential disk from the surface brightness, a central emission excess remains at $R \lesssim 0.5$ kpc (Bothun 1992, Regan & Vogel 1994) which has been attributed to spiral arms, to an extended semistellar nucleus or to a diffuse halo or bulge. We shall refer to this excess as the “nucleus” of M33 despite the fact that in the literature the word “nucleus” is often used for the light excess observed only at $R \lesssim 10$ pc (Kormendy & McClure 1993). Nuclear rotational velocities have been observed in H α along the major axis between 20 and 200 pc from the center (Rubin & Ford 1985), and seem roughly constant at about ~ 27 km s $^{-1}$. This flatness of the rotation curve is quite puzzling and needs further investigation once uncertainties on the nuclear rotational velocities will be established together with a knowledge of the velocity field along different directions. In this paper we model the rotation curve at $R \gtrsim 150$ pc only, considering two different possibilities for the nuclear component V_n at these radii:

(1) $V_n \propto R^{0.5}/(R + a)$. This rotational velocity approximates the dynamical contribution of a spheroidal mass distribution whose surface density can be fitted by a de Vaucouleurs $R^{1/4}$ law (Hernquist 1990). This scaling law has been used by Regan & Vogel (1994) to fit the J-band nuclear surface brightness. The compatibility of the fit with photometric data in other bands (e.g. Bothun 1992) is somewhat uncertain, as is the value of the scalelength a . Suggested values of a lie in the range $0.1 \leq a \leq 1$ kpc, which we will consider in this paper.

(2) $V_n \propto R^{-0.115}$, as if core collapse has happened or is happening in the compact stellar nucleus (Cohn 1980, Kormendy & McClure 1993). The corresponding power-law mass density distribution develops up to a limiting outer radius R_c , which should also be given. For $R > R_c$, $V_n \propto R^{-0.5}$. We consider as possible R_c values the radius of each data point of the rotation curve inside the optical region i.e. $R_c < 8$ kpc. We consider also the case $R_c \ll 150$ pc, which is appropriate if most of the

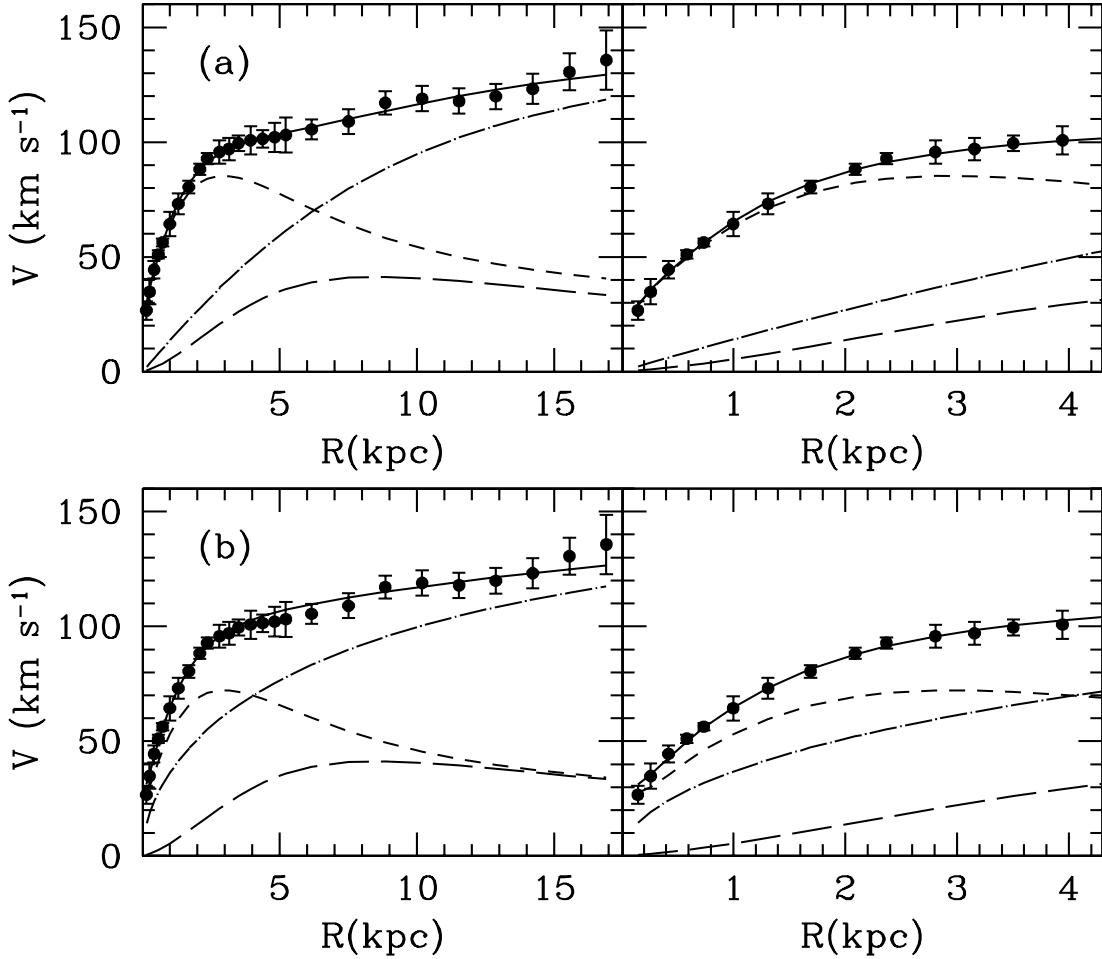


Figure 5. The M33 rotation curve (points). (a) The best-fitting model (solid line) using Burkert profile for the dark halo density distribution, and the nuclear model (1). Also shown are the dark halo contribution (dot-dashed line), the stellar disk + nucleus (short-dashed line) and the gas contribution (long-dashed line). (b) The same as in (a) but for NFW dark halo profile with $C_{100} = 8$ and the nuclear model (2). The left panels show an enlargement of the inner fit.

nuclear mass resides at very small radii and the nucleus can be treated as a point source throughout the extent of the present rotation curve.

Hereafter, we will refer to these models as nuclear model (1) and (2) respectively. It has been established by CS that the visible baryons in M33 are only a small fraction of the total galaxy mass, and that a dark matter halo is in place. We will use the M33 rotation curve presented here to test in details the consistency of the required halo density profile with theoretical models which predict a well defined dark matter distribution around galaxies. Namely, in addition to the widely used non-singular isothermal dark halo model we shall consider a spherical halo with a dark matter density profile as originally derived by Navarro Frenk and White (1996, 1997, hereafter NFW) for galaxies forming in a Cold Dark Matter scenario (hereafter CDM). We consider also the Burkert and the Moore dark matter density profile (Burkert 1995, Moore et al. 1998). All models have two free parameters to be determined from the rotation curve fit. The density distribution for a non-singular isothermal dark halo can be written as:

$$\rho(R) = \frac{\rho_{iso}}{1 + \left(\frac{R}{R_{iso}}\right)^2} \quad (3)$$

The density profile proposed by Burkert (1995) has also a flat density core:

$$\rho(R) = \frac{\rho_B}{\left(1 + \frac{R}{R_B}\right)\left(1 + \left(\frac{R}{R_B}\right)^2\right)} \quad (4)$$

and a strong correlation between the two free parameters ρ_B and R_B has been found by fitting the rotation curve of low mass disk galaxies.

The NFW density profile is:

$$\rho(R) = \frac{\rho_{NFW}}{\frac{R}{R_{NFW}}\left(1 + \frac{R}{R_{NFW}}\right)^2} \quad (5)$$

Numerical simulations of galaxy formation in CDM models find a correlation between ρ_{NFW} and R_{NFW} which depends on the cosmological model (Avila-Reese et al. 2001, Eke Navarro and Steinmetz 2001). Often this correlation is expressed using the concentration parameter $C_\Delta \equiv R_\Delta/R_{NFW}$ and M_Δ or V_Δ . R_Δ is the radius of a sphere containing a mean density Δ times the critical density, V_Δ and M_Δ are the characteristic velocity and mass inside R_Δ . We use a Hubble constant $H_0 = 65 \text{ km s}^{-1} \text{ Mpc}^{-1}$ and show results for $\Delta = 100$, as in CDM halo models of Eke Navarro and Steinmetz (2001), unless otherwise specified.

A similar profile but with a different central slope has been suggested instead by numerical simulations of Moore et al. (1998) for galaxies forming in CDM scenarios:

$$\rho(R) = \frac{\rho_M}{\left(\frac{R}{R_M}\right)^{1.5}\left(1 + \left(\frac{R}{R_M}\right)^{1.5}\right)} \quad (6)$$

For each dark halo model and each nuclear model we shall determine five free parameters applying the least-square method to the observed rotation curve. These free parameters are: the dark halo core radius $R_{iso,NFW,M,B}$, the dark matter density ρ_{opt} computed at $R = R_{opt} \equiv 3.2R_d \simeq 4.1 \text{ kpc}$, the ratio between the stellar disk mass M_d and the blue luminosity of the galaxy L ($L \simeq 5.7 \times 10^9 L_\odot$), the nuclear mass M_n , and the nuclear scale length a or the cut-off radius R_c . The 1- σ , 2- σ and 3- σ ranges are determined using the reduced χ^2 and assuming Gaussian statistics. They are computed by determining in the free parameters space the projection ranges, along each axis, of the hypersurfaces corresponding to the 68.3%, 95.4% and 99.7% confidence levels.

Both the non-singular isothermal dark halo model and the Burkert dark matter density profile give good fits to the rotation curve since the minimum reduced χ^2 is 0.7 for the nuclear model (1) and 1.2 for the nuclear model (2). The best fitting values of the free parameters are: $a = 0.4 \text{ kpc}$, $M_n = 3 \times 10^8 M_\odot$, $M_d/L = 1 M_\odot/L_\odot$, $R_{iso} = 7 \text{ kpc}$ or $R_B = 12 \text{ kpc}$, $\rho_{opt} = 5 \times 10^{-25} \text{ g cm}^{-3}$ for the nuclear model (1), and $R_c = 0.7 \text{ kpc}$, $M_n = 10^8 M_\odot$, $M_d/L = 1 M_\odot/L_\odot$, $R_{iso} = 8 \text{ kpc}$ or $R_B = 13 \text{ kpc}$, $\rho_{opt} = 5 \times 10^{-25} \text{ g cm}^{-3}$ for the nuclear model (2). The 3- σ ranges for the free parameters of both the isothermal and the Burkert model are:

$$0.8 \leq \frac{M_d/L}{M_\odot/L_\odot} \leq 1.1; \quad 5 \times 10^7 \leq \frac{M_n}{M_\odot} \leq 8 \times 10^8; \quad 4 \times 10^{-25} \leq \frac{\rho_{opt}}{\text{g cm}^{-3}} \leq 7 \times 10^{-25};$$

$$0.4 \leq \frac{R_c}{\text{kpc}} < 8; \quad 7 \leq \frac{R_B}{\text{kpc}} \leq 19 \quad \text{or} \quad 4 \leq \frac{R_{iso}}{\text{kpc}} \leq 13.$$

The resulting 3- σ range for the nuclear scale length a in the nuclear model (1) covers the whole range we have considered i.e. $0.1 \leq a \leq 1 \text{ kpc}$. For the nuclear model (2) instead we find a lower limit to R_c . This means that the nucleus cannot be considered a point source for any possible dark halo models we are examining. This ‘dynamical’ conclusion agrees with photometric data (Bothun 1992, Minniti, Olszewski & Rieke 1993, Regan & Vogel 1994) showing an excess of light inward of 0.5 kpc after subtracting the exponential disk. Unfortunately estimates of the nuclear luminosity L_n are still quite uncertain: in the B-band $7 \times 10^7 \leq L_{n,B} \leq 3 \times 10^8 L_{\odot,B}$ (Bothun 1992, Regan & Vogel 1994), and we cannot limit the nuclear stellar mass range further based on possible unrealistic values of the mass to light ratio (Bell & de Jong 2001). An extended nucleus is not required instead if the density of the dark matter scales as $R^{-1.3 \pm 0.1}$ throughout the halo; these type of solutions has been investigated by CS and provides also good fits to the rotation data presented in this paper. Both the Burkert and the isothermal model require a very extended core region of nearly constant dark matter density. Figure 5(a) shows the best fit using the Burkert profile with the nuclear model (1). The 1- σ and 3- σ probability contours for $a = 0.4 \text{ kpc}$ in the $\rho_{opt} - R_B$ plane are displayed in Figure 6(a). The correlation found by Burkert between ρ_B and R_B implies a relation between ρ_{opt} and R_B shown with crosses in Figure 6(a). We can see that the M33 acceptable parameters lie close to, but outside, the Burkert correlation line. So either the found scaling relation between ρ_{opt} and R_B should be slightly modified to include M33, or it changes for values of R_B larger than those considered by Burkert. A Burkert model which fits M33 is indistinguishable from an isothermal model since both require a large constant density core region and, even at the outermost fitted radius, the dark matter density does not decline yet as an R^{-2} or R^{-3} power law. The dark matter density profile suggested by Moore fails to fit the observed rotation curve in M33.

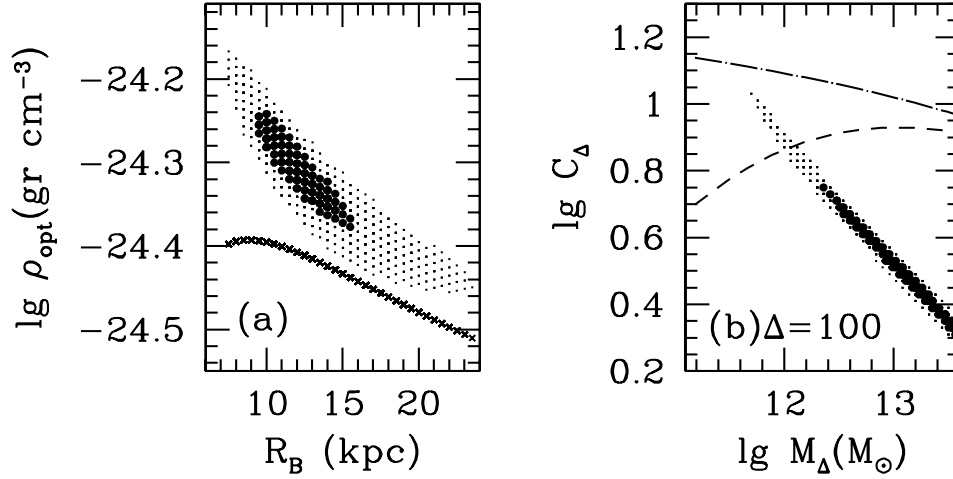


Figure 6. (a) The light dots indicate the 3- σ confidence area for the Burkert dark halo model in the R_B $\lg(\rho_{opt})$ plane; the heavy dots are for the 1- σ confidence area. The cross line indicates the correlation found by Burkert. The 3- σ (light dots) and 1- σ (heavy dots) confidence areas for the NFW dark halo model are shown in (b) in the $\lg(M_\Delta)$ - $\lg(C_\Delta)$ plane for $\Delta=100$. The dashed and dashed-dotted lines indicate the numerical simulation results for model W_8 and $S_{0.9}$ respectively of Eke, Navarro & Steinmetz (2001).

For the NFW dark matter density profile for $\Delta = 100$ or 200 the minimum χ^2 is 0.7 for the nuclear model (1) and 1.0 for the nuclear model (2). The best fitting values of the free parameters for the nuclear model (1) are: $a = 0.4$ kpc, $M_n = 2 \times 10^8 M_\odot$, $M_d/L = 0.8 M_\odot/L_\odot$, $R_{NFW} = 140$ kpc, $\rho_{opt} = 6 \times 10^{-25} \text{ g cm}^{-3}$. For the nuclear model (2) $R_c = 0.7$ kpc, $M_n = 8 \times 10^7 M_\odot$, $M_d/L = 0.8 M_\odot/L_\odot$, $R_{NFW} = 300$ kpc, $\rho_{opt} = 6 \times 10^{-25} \text{ g cm}^{-3}$. The 3- σ ranges for the free parameters are:

$$0.5 \leq \frac{M_d/L}{M_\odot/L_\odot} \leq 0.9; \quad 3 \times 10^7 \leq \frac{M_n}{M_\odot} \leq 4 \times 10^8; \quad 5 \times 10^{-25} \leq \frac{\rho_{opt}}{\text{g cm}^{-3}} \leq 8 \times 10^{-25};$$

$$0.3 \leq \frac{R_c}{\text{kpc}} < 8; \quad \frac{R_{NFW}}{\text{kpc}} > 15$$

The corresponding 3- σ upper limit for the concentrations is $C_{100} < 12.5$ for nuclear model (1) and $C_{100} < 11$ for nuclear model (2), while the corresponding best fits to the rotation curve require $C_{100} \simeq 4$ and $C_{100} \simeq 2.5$ respectively. For all the dark halos we are examining the nuclear model (2) provides a flatter rotation curve than model (1) inward of the center-most data point fitted, in agreement with the preliminary measures of Rubin & Ford (1985). The central steepness of the NFW dark matter density profile lowers the nuclear stellar mass required to fit the rotational data. Figure 6(b) shows the 1- σ and 3- σ areas in the $M_{100} - C_{100}$ plane. The dashed and dashed-dotted lines in the same figure are the fits to numerical simulation results for structures formation in the cosmological models W_8 and $S_{0.9}$ respectively of Eke, Navarro & Steinmetz (2001). Both model assume matter density parameters $\Omega_0 = 0.3$ and $\Lambda_0 = 0.7$, a power spectrum in the form given by Bardeen et al. (1986) with $\sigma_8=0.9$ and shape parameter $\Gamma = 0.2$. $S_{0.9}$ corresponds to this ‘standard’ Λ CDM spectrum, while W_8 mimics a Warm Dark Matter power spectrum because in addition its power is reduced on scales smaller than that of the characteristic free streaming mass $M_f = 8 \times 10^{11} M_\odot$. It can be easily seen in Figure 6(b) that the possible C_Δ and M_Δ values for M33 are consistent with a Warm Dark Matter cosmology but lie below the relation found in simulated standard CDM halos. These $M_\Delta - C_\Delta$ relations have however an associated scatter. Even a small scatter, $\sigma(\lg C_\Delta)=0.1$ as suggested for galaxies which did not undergo major mergers (Wechsler et al. 2002), makes the M33 dark halo still compatible with standard Λ CDM galaxy formation models. We display in Figure 5(b) the fit to the M33 rotation curve using a NFW dark halo profile with $C_{100} = 8$, compatible with a standard Λ CDM and a Warm Dark Matter cosmology. The nuclear model (2) is used. The reduced χ^2 and the values of the free parameters found from the best fit are: $\chi^2 = 1.5$, $R_c = 0.7$ kpc, $M_n = 7.5 \times 10^7 M_\odot$, $M_d/L = 0.7 M_\odot/L_\odot$, $R_{NFW} = 35$ kpc, $\rho_{opt} = 7 \times 10^{-25} \text{ g cm}^{-3}$.

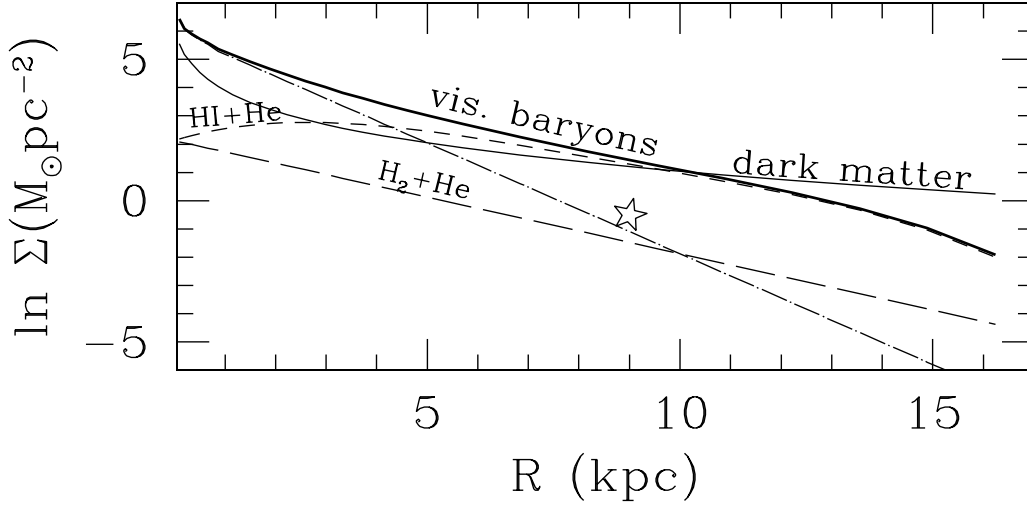


Figure 7. The surface density of baryonic and dark matter in M33. The mass model used for Figure 5(b) has been used here to compute the stellar contribution from the nucleus and the disk (dot-dashed line) and the dark matter surface density within 0.5 kpc height from the galactic plane (continuous line). The short dashed line is the HI+He surface density, the long-dashed line is the H₂+He surface density, the solid heavy line is the sum of the two and of the stellar surface density.

5 SURFACE DENSITIES OF VISIBLE MATTER AND THE GLOBAL STABILITY OF THE DISK

In the previous Section we have determined the dark matter and stellar contribution to the M33 rotation curve. Despite the fact that the radial scaling law of the dark matter density required for fitting the rotation curve is not unique, the total baryonic and dark mass up to the last measurable point ($R=17$ kpc) are determined with small uncertainties. The total stellar mass in the M33 disk is estimated to be $3\text{--}6 \times 10^9 M_{\odot}$. The mass of the dark halo at the outermost observable radius is about a factor 10 higher than the stellar disk mass. The neutral hydrogen plus the molecular gas mass is $2.4 \times 10^9 M_{\odot}$. We don't have a firm estimate of the nuclear stellar mass M_n , but all three possible dark matter models discussed in this paper require an extended distribution. Its mass lies in the range $5 \times 10^7 \leq M_n \leq 8 \times 10^8 M_{\odot}$ if the dark halo has a large size core of constant density, while $3 \times 10^7 \leq M_n \leq 4 \times 10^8 M_{\odot}$ if the dark halo has a central cusp as in NFW model. We can estimate the total surface density of visible baryons in M33 neglecting at the moment the small contribution from the ionized gas. Figure 7 shows the total baryonic surface density computed by adding the helium to the molecular and the neutral atomic gas (a 1.33 factor correction), and adding to this the nuclear and stellar disk surface density. We use the mass model displayed in Figure 5(b), for which we show also the dark matter surface density within 0.5 kpc from the plane of the galaxy. We extrapolate the fits of the stellar and molecular gas surface density out to 16 kpc but it is likely they experience a truncation at smaller radii. For the HI surface density only we know that it declines sharply beyond 15-16 kpc due to ionization effects by an extragalactic background (Corbelli & Salpeter 1993). The gas distribution is likely to extend further out but the dominant phase becomes ionized atomic hydrogen. Assuming a gaseous vertical extent of 0.5 kpc above and below the galactic plane, we can say that the surface density of visible baryons falls below the dark matter surface density contained in the M33 disk for $R \gtrsim 10$ kpc. A similar conclusion applies also for the Burkert best fit model.

Using our accurate measurement of the rotational velocity gradient and of the surface density of the baryonic and non baryonic components, we can check if the onset of massive star formation in M33 is strongly related to a global instability of the disk. One of the most popular tools used to assess the gravitational stability of gaseous disks is the Toomre stability criterion:

$$f\Sigma_g < \Sigma_T \equiv \frac{\kappa c_g}{\pi G} \quad (7)$$

where Σ_g is the gas surface mass density, f is the disk thickness factor, κ is the epicyclic frequency (Toomre 1964), G is the gravitational constant, c_g is the gas velocity dispersion. We shall use both $f = 1$ as for a thin disk and $f = 0.7$ to mimic instead a disk with a finite thickness (Romeo 1992). The criterion described by equation (7) is not at all related to the star formation efficiency but it correctly predicts the occurrence of a star formation threshold radius which, in many spiral galaxies, has been determined from the drop of the H α surface brightness (e.g. Martin & Kennicutt 2001). In M33 Kennicutt (1989) observed such a drop at $R_* \simeq 6.4$ kpc. However, since the early work of Kennicutt it is well known that the simple Toomre stability

criterion fails to account for the active star forming region in the disk of low mass spirals such as M33 (Elmegreen 1993, van Zee et al. 1997, Wong & Blitz 2002). An alternative stability criterion includes the shear rate of the disk and it may be more appropriate for irregular galaxies (Elmegreen 1993, Hunter Elmegreen & Baker 1998). It is based on the consideration that making new stars is possible only when there is enough time for the instability to grow, before shear stretches the perturbation apart. This corresponds to the following condition:

$$f\Sigma_g < \Sigma_A \equiv \frac{2.5Ac_g}{\pi G} \quad (8)$$

where the Oort constant $A = -0.5Rd\Omega/dR$ is the local shear rate. In Figure 8 we display Σ_T and Σ_A , using $c_g = 6 \text{ km s}^{-1}$. This value is at the lowest end of the cold gas velocity dispersion range estimated in M33 (6-9 km s^{-1} , Warner et al. 1973, Thilker 2000). The thin and thick continuous lines in Figure 8 show the mass surface densities for $f = 1$ and for $f = 0.7$ respectively. The arrow indicates R_* . We can see in Figure 8(a) that at $R \simeq R_*$ the azimuthally averaged surface gas density for a thin disk falls below the threshold for a gravitational instability to develop according to the shear rate criterion. We shall investigate now if considering additional sources of gravity in the disk, a modified version of the classical Toomre criterion can still give correct predictions for the star formation threshold radius.

Since the masses of stars and gas in the M33 disk are comparable, we are encouraged to use a stability parameter for a two components fluid. Following Wang & Silk (1994) we define $\Sigma_* \equiv \Sigma_s \times c_g/c_s$, where Σ_s and c_s are the surface density and velocity dispersion of the stars in the disk. Using the epicyclic frequency or the shear rate of the disk, the stability condition reads:

$$f(\Sigma_g + \Sigma_*) < \Sigma_T, \Sigma_A \quad (9)$$

Figure 8(b) shows $f(\Sigma_g + \Sigma_*)$, using $M_d/L = 0.7 M_\odot/L_\odot$ for deriving Σ_* (as for the mass model shown in Fig. 5(b)), and $c_g/c_s = 0.3$. For $c_g = 6 \text{ km s}^{-1}$ this last ratio implies $c_s = 20 \text{ km s}^{-1}$, a value observed in the central regions of M33 (Kormendy and McClure 1993, Gebhardt et al. 2001). We can see that with a value of M_d/L slightly higher than 0.7, the Toomre criterion for a thin disk predicts correctly a gravitationally unstable disk for $R < R_*$. If finite thickness effects are taken into account or if c_g is higher than 6 km s^{-1} at $R \simeq R_*$ we need the shear rate criterion.

Following Hunter, Elmegreen & Baker (1998) we consider also the possible influence of dark matter gravity. If Σ_{dm} is the dark matter surface density within the vertical extent of the gas, we can rewrite equation (9) as

$$f(\Sigma_g + \Sigma_{dm} + \Sigma_*) < \Sigma_T, \Sigma_A \quad (10)$$

In Figure 8(c) we show $f(\Sigma_g + \Sigma_{dm} + \Sigma_*)$ assuming a gaseous extent of 0.5 kpc above and below the galactic plane and a NFW dark matter profile as used for the rotation curve fit displayed in Figure 5(b). In this case finite thickness effects, or equivalently a velocity dispersion as high as 9 km s^{-1} , make the disk gravitationally unstable, according to the Toomre criterion, exactly for $R < R_*$. This solution is not unique. If the gas is in hydrostatic equilibrium for example, the gas vertical extension and the velocity dispersion are not independent variables. An approximation to the scale height of the gas for a galactic disk of stars and gas in hydrostatic equilibrium in a dark matter halo is given by

$$h_g = \frac{c_g}{\pi G} \left(\frac{\Sigma_g + \Sigma_{dm}}{c_g} + \frac{\Sigma_s}{c_s} \right)^{-1} \quad (11)$$

Since Σ_{dm} is the dark matter surface density between $+h_g$ and $-h_g$ the above formula should be solved numerically for determining h_g and Σ_{dm} . In Figure 8(d) we plot $f(\Sigma_g + \Sigma_{dm} + \Sigma_*)$, for Σ_{dm} between $\pm h_g$ for the same dark matter density used in Figure 8(c). We find that h_g varies between 20 pc and 1 kpc through the radial extent of the disk analyzed in this paper. This model reduces the radii of the unstable star forming regions respect to the constant scale height model displayed in Figure 8(c), making both Σ_A and Σ_T suitable indicators of the growth of instabilities in the disk. Which one it is better to use for defining a threshold radius in M33 is therefore still unclear since this depends on the radial variations of the involved parameters such as sound speed, thickness etc. which are not well determined yet. It is important to notice however that since the densities of visible baryons and dark matter are well constrained at intermediate radii, the intersections between Σ_A or Σ_T and $f(\Sigma_g + \Sigma_{dm} + \Sigma_*)$ do not depend on which mass model we use, as soon as it is compatible with the rotational velocity data. The Burkert best fitting mass model, for example, gives the same solutions displayed in Figure 8 for a NFW dark matter halo.

6 SUMMARY

A full map of the nearby galaxy M33 in the CO J=1-0 transition has given additional data for improving the accuracy of the rotation curve of this galaxy and the knowledge of the visible baryons distribution. The molecular gas peaks in the central regions with a surface density of about $7 M_\odot \text{ pc}^{-2}$ and declines exponentially with a radial scalelength of about 2.5 kpc down to about $0.6 M_\odot \text{ pc}^{-2}$ at $R \simeq 6 \text{ kpc}$. Our sensitivity was not sufficient to outline the molecular gas radial distribution

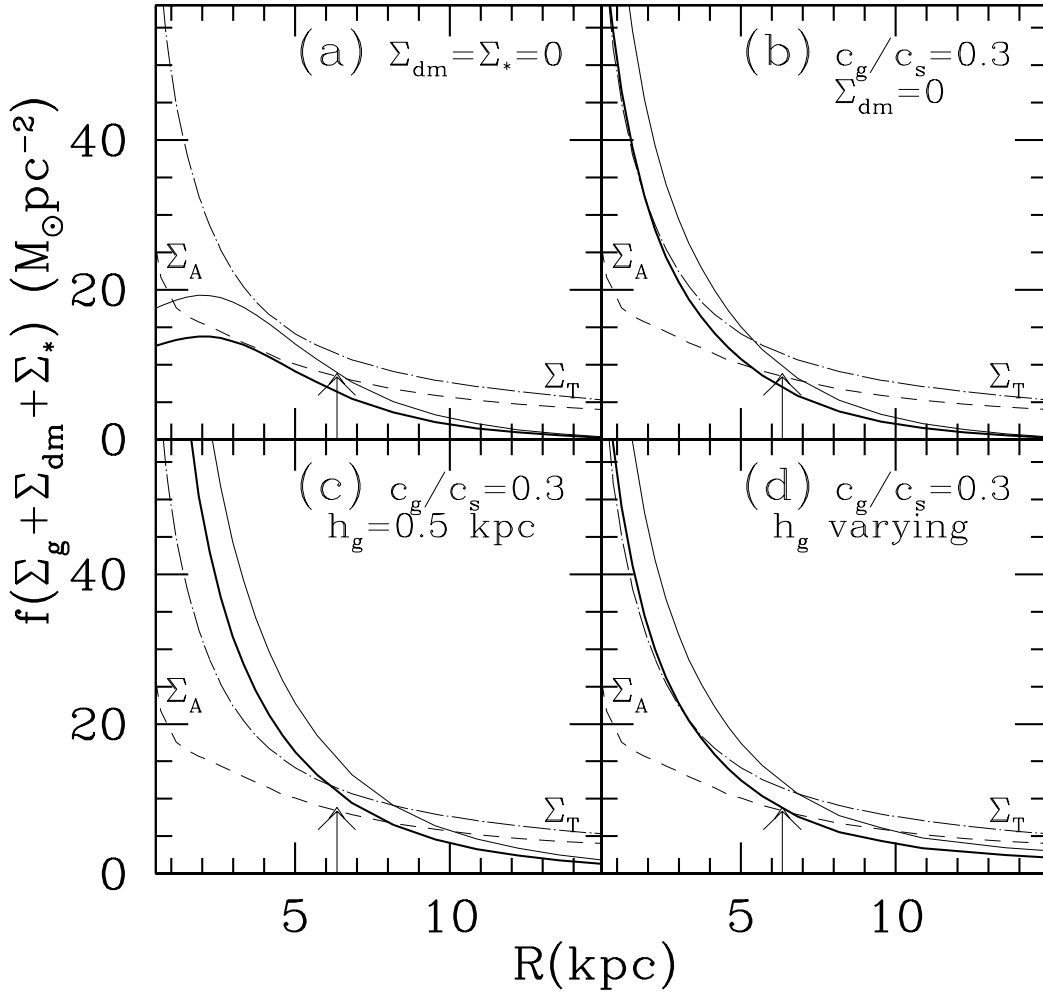


Figure 8. The stability of the M33 disk for $c_g = 6 \text{ km s}^{-1}$. The dashed-dotted line and the dashed line in each panel show Σ_T and Σ_A respectively, as a function of radius. An arrow has been placed at the observational value of R_* . The thin and thick continuous lines are for $f = 1$ and $f = 0.7$ respectively. We plot $f\Sigma_g$ in (a) and $f(\Sigma_g + \Sigma_*)$ in (b) for $M_d/L = 0.7$ and. In (c) we add the dark matter surface density within a 0.5 kpc layer above and below the galactic plane, while in (d) the dark matter is computed within a radially varying vertical height of the gas (see text for details).

further out and in particular to detect any possible sudden drop of the azimuthally averaged molecular gas surface density. The molecular gas is not smoothly distributed in the inner disk since there are remarkable mass concentrations along the spiral arms. Some wiggles of about 10 km s^{-1} are visible in the rotation curves of the two separate halves of the galaxy, which are reminiscent of density wave perturbations. Details of atomic and ionized gas distribution in M33 can be found in Hoopes & Walterbos (2000) and in Thilker, Braun & Walterbos (2001). The rotation curve derived using $H\alpha$ data for the innermost point, the CO data and the HI 21-cm line data, has been used to constrain the visible baryonic mass and dark matter halo models. The total gas mass (HI+H₂+He) is $\sim 3.2 \times 10^9 M_\odot$. This is of the same order of the stellar disk mass, estimated to be between 3×10^9 and $6 \times 10^9 M_\odot$. The total visible baryonic mass of M33 can therefore be as high as $10^{10} M_\odot$. The dark halo mass out to the last measured point (17 kpc from the center) is $\sim 5 \times 10^{10} M_\odot$.

Both the non-singular isothermal halo and the Burkert halo model, give good fits to the M33 rotation curve when the flat density core is extended. The pure R^{-2} or R^{-3} outer scaling law applies only beyond the outermost observed radius. Dark matter density profiles with an inner $R^{-1.5}$ cusp (Moore et al. 1998) are too steep to be consistent with the rotation of the central regions of M33 and are ruled out. Halo models with milder central cusps, such as the NFW radial profile, fit well all the observed rotational velocities. The mass of the virialized NFW dark halo for this galaxy is $\geq 5 \times 10^{11} M_\odot$ and the halo size comparable to the distance between M33 and its bright companion M31 ($\sim 180 \text{ kpc}$). The baryon fraction in M33 is then ≤ 0.02 . The required concentrations C_Δ are below the scaling laws found by numerical simulations of structures formation

in a standard Cold Dark Matter scenario ($\Omega_0 = 0.3$, $\Lambda_0 = 0.7$, $\sigma_8=0.9$) and favor cosmological models which predicts less concentrated dark halos (Eke, Navarro & Steinmetz 2001, Zentner & Bullock 2002, van den Bosch, Mo & Yang 2003). We have shown however that if an associated scatter in the numerical simulation results is considered (Wechsler et al. 2002), the M33 dark halo is still compatible with galaxy formation models in a standard Λ CDM cosmology. The finding that dark matter halos are consistent with constant density core models or with central cusps less steep than $R^{-1.5}$, is known as the cusp-core degeneracy (van den Bosch & Swaters 2001). It is remarkable that this degeneracy holds also in M33 which is a galaxy with small uncertainties about its distance, its gaseous and stellar content, and with circular velocities sampled over a wide range of radii: from galactocentric distances of a few parsecs out to 13 disk scalelengths. For this galaxy it seems that the degeneracy holds mostly because of a nuclear stellar component, which regulates the dynamics of the innermost 0.5 kpc region. This extended ‘stellar nucleus’, with mass between 3×10^7 and $8 \times 10^8 M_\odot$, is not only dynamically required by the rotational data but it is also evident from photometric data (Bothun 1992, Minniti, Olszewski & Rieke 1993, Regan & Vogel 1994). We have considered a core collapse model and a de Vaucouleurs $R^{1/4}$ law for the nuclear stellar density but additional data on the kinematics and light distribution of the central few hundreds parsec region are needed to constrain better the mass distribution there.

Having a very accurate rotation curve and a good estimate of the gas, stellar and dark matter surface density in the M33 disk, we have addressed the question on the possible coincidence of the active star formation region in this galaxy with a gravitationally unstable region. Azimuthal averages of the observed gas surface densities are above the critical densities in the star forming region of M33 only if one considers the minimum acceptable value of the gas velocity dispersion and a stability criterion based on the shear rate of the disk. However, the simple Toomre condition predicts a star formation threshold radius in agreement with the observed drop in the $H\alpha$ surface brightness if the additional compression due to the stellar disk or to the dark matter surface density is considered.

I acknowledge Steve Schneider and Mark Heyer for having given me the opportunity to use the CO data prior to publication. I am also very thankful to the anonymous referee who made several excellent suggestions for improving the quality of the work presented in the original manuscript.

REFERENCES

- Alam S. M. K., Bullock J. S., Weinberg D. H. 2002, ApJ, 572, 34
 Avila-Rees V., Colin P., Valenzuela O., D’Onghia E., Firmani C., 2001, ApJ, 559, 516
 Bardeen J. M., Bond J. R., Kaiser N., Szalay A. S. 1986, ApJ, 304, 15
 Bell E. F., de Jong R. S. 2001, ApJ, 550, 212
 Bolatto A. D., Simon J. D., Leroy A., Blitz L. 2002, ApJ, 565, 238
 Bothun G. D. 1992, AJ, 103, 104
 Burkert A., 1995, ApJL, 447, L25
 Cohn H., 1980, ApJ, 242, 765
 Corbelli E., 2000, in Berkhuijsen E. M., Beck R., Walterbos R. A. M., eds, The ISM in M31 and M33, Shaker Verlag, p. 11
 Corbelli E., Salpeter E. E., 1993, ApJ, 419, 104
 Corbelli E., Schneider S. E., 1997, ApJ, 479, 244
 Corbelli E., Salucci P., 2000, MNRAS, 311, 441 (CS)
 Elmegreen B. G., 1993, in Franco J., Ferrini F., Tenorio-Tagle G., eds, Star Forming galaxies and their ISM, Cambridge, p. 106
 Eke V. R., Navarro J. F., Steinmetz M., 2001, ApJ, 554, 114
 Freedman W. L. et al. 2001, ApJ, 553, 47
 Gebhardt K. et al., 2001, AJ, 122, 2469
 Hernquist L., 1990, ApJ, 356, 359
 Heyer M. H., Corbelli E., Schneider S. E., 2003, in preparation
 Hoopes, C.G., Walterbos, R.A.M., 2000, ApJ, 541, 597
 Hunter D. A., Elmegreen B. G., Baker A. L., 1998, ApJ, 493, 595
 Kennicutt R. C., 1989, ApJ, 344, 685
 Kormendy J., McClure R. D., 1993, AJ, 105, 1793
 Martin C. L., Kennicutt R. C., 2001, ApJ, 555, 301
 Minniti D., Olszewski W., Rieke M. 1993, ApJL, 410, L79
 Moore B., Governato F., Quinn T., Stadel J., Lake G., 1998, ApJL, 499, L5
 Navarro J. F., Frenk C. S. F., White S. D. M., 1996, ApJ, 462, 563
 Navarro J. F., Frenk C. S. F., White S. D. M., 1997, ApJ, 490, 493
 Newton K., 1980, MNRAS, 160, 689
 Persic M., Salucci P., Stel P., 1996, MNRAS, 281, 27
 Regan M. W., Vogel S. N., 1994, ApJ, 434, 536
 Romeo A. B. 1992, MNRAS, 256, 307
 Rubin V. C., Ford W. K., 1985, Carnegie Inst. Washington Ann. Rept., No. 85, p. 66
 Thilker D. A., 2000, in Berkhuijsen E. M., Beck R., Walterbos R. A. M., eds, The ISM in M31 and M33, Shaker Verlag, p. 3
 Thilker D. A., Braun R., Walterbos R. A. M., 2001, in Hibbard J. E., Rupen M., van Gorkom J. H. eds, Gas and Galaxy Evolution, ASP Vol. 240, p. 456

- Toomre A., 1964, ApJ, 139, 1217
van den Bosch F. C., Swaters R. A., 2001, MNRAS, 325, 1017
van den Bosch F. C., Mo H. J., Yang X. 2003, MNRAS, submitted (astro-ph/0301104)
van Zee L., Haynes M. P., Salzer J. J., Broeils A. H. 1997, AJ, 113, 1618
Wang B., Silk J., 1994, ApJ, 427, 759
Warner P. F., Wright M. C. H., Baldwin F. E., 1973, MNRAS, 163, 163
Wechsler R. H., Bullock J. S., Primack J. R., Kravtsov A. V., Dekel A., 2002, ApJ, 568, 52
Wilson C. D., 1995, ApJL, 448, L97
Wilson C. D., Scoville N., 1989, ApJ 347, 743
Wong T., Blitz L., 2002, ApJ, 569, 157
Zentner A. R., Bullock J. S., 2002, PhRvD, 66, 3003